Published in final edited form as:
Acc Chem Res. 2011 October 18; 44(10): 914–924. doi:10.1021/ar200061q.

Gold Nanocages: From Synthesis to Theranostic Applications

YOUNAN XIA[*], **WEIYANG LI**, **CLAIRE M. COBLEY**, **JINGYI CHEN**, **XIAOHU XIA**, **QIANG ZHANG**, **MIAOXIN YANG**, **EUN CHUL CHO**, and **PAIGE K. BROWN**
Department of Biomedical Engineering, Washington University, Saint Louis, Missouri 63130

CONSPECTUS

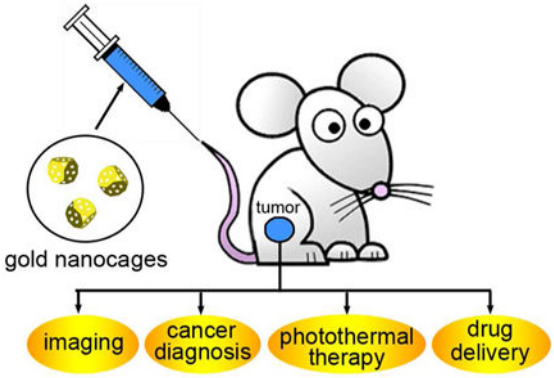

Gold nanostructures have garnered considerable attention in recent years for their potential to enhance both the diagnosis and treatment of cancer through their advantageous chemical and physical properties. The key feature of Au nanostructures for enabling this diverse array of biomedical applications is their attractive optical properties, i.e. the scattering and absorption of light at resonant wavelengths due to the excitation of plasmon oscillations. This phenomenon is commonly known as localized surface plasmon resonance (LSPR) and is the source of the ruby red color of conventional Au colloids. The resonant wavelength is highly dependent on the size, shape, and geometry of the nanostructures, providing a set of knobs to maneuver the optical properties as needed. For *in vivo* applications, especially when optical excitation or transduction is involved, the LSPR peaks of the Au nanostructures have to be tuned to the transparent window of soft tissues in the near-infrared (NIR) region (from 700–900 nm) in order to maximize the penetration depth.

One class of nanostructures with tunable LSPR peaks in the NIR region is Au nanocages. These versatile nanostructures are characterized by hollow interiors, ultrathin and porous walls, and can be prepared in relatively large quantities using a remarkably simple procedure based on the galvanic replacement between Ag nanocubes and aqueous chloroauric acid. The LSPR peaks of Au nanocages can be readily and precisely tuned to any wavelength in the NIR region by controlling their size and/or wall thickness. Other significant features of Au nanocages that make them particularly intriguing materials for biomedical applications include their compact sizes, large absorption cross sections (almost five orders of magnitude greater than those of conventional organic dyes), bio-inertness, as well as a robust and straightforward procedure for surface modification based on the Au-thiolate chemistry. In this article, we present some of the most recent advances in the use of Au nanocages for a broad range of theranostic applications, including their use: *i*) as tracers for tracking by multi-photon luminescence; *ii*) as contrast agents for photoacoustic (PA) and mutimodal (PA/fluorescence) imaging; *iii*) as photothermal agents for the

[*]Corresponding author. xia@biomed.wustl.edu.

selective destruction of cancerous or diseased tissue; and *iv*) as drug delivery vehicles for controlled and localized release in response to external stimuli such as NIR radiation or high-intensity focused ultrasound (HIFU).

Introduction

Gold nanostructures provide a versatile, multifaceted platform for a broad range of biomedical applications.[1] Recent studies have validated their use in a number of techniques for both cancer diagnosis and therapies. For example, they can serve as substrates for the detection of trace biomarkers using spectroscopic methods; they can function as contrast agents for a number of optical imaging modalities; they can act as carriers for the delivery and controlled release of drugs; and they can serve as transducers for the photothermal destruction of tumor cells.

Most of these applications are based upon an optical phenomenon known as localized surface plasmon resonance (LSPR). When a Au nanostructure is illuminated with an electromagnetic wave, its conduction electrons will be driven by the electric field to collectively oscillate relative to the lattice of positive ions, creating intense peaks (both scattering and absorption) at resonant wavelengths. For *in vivo* applications, Au nanostructures must have LSPR peaks in the near-infrared (NIR) region ranging from 700–900 nm. In this so-called transparent window, light can penetrate deeply into soft tissues due to a great reduction in absorption from hemoglobin and water in the blood and in scattering by the tissue.[2] For conventional Au colloids with a solid structure and a spherical shape, their LSPR peaks are typically limited to the visible region. Only those Au nanostructures with specific nonspherical morphologies (e.g., rod, rice, multipod, and star) or a hollow structure (e.g., shell, box, and cage) can have LSPR peaks in the NIR region.[1] While nanostructures made of other metals can also exhibit strong LSPR, the non-reactive and relatively bio-inert nature of Au makes this metal the most prominent candidate for both *in vitro* and *in vivo* applications. In fact, ^{198}Au colloids were used in human trials in the 1950's as radioactive tracers for sentinel lymph node biopsy.[3] Recently, Au nanoparticles have been tested in a phase-I clinical trial for tumor-targeted drug delivery.

Gold nanocages (AuNCs) represent a novel class of nanostructures invented by our group in 2002.[4] They can be prepared using a remarkably simple synthetic route that involves galvanic replacement between Ag nanocubes and $HAuCl_4$ in an aqueous solution.[5] In addition to their obvious features, such as hollow interiors and porous walls, AuNCs have a range of hidden qualities that make them unique for theranostic applications: *i*) they are single crystals with good mechanical flexibility and stability, as well as atomically flat surfaces; *ii*) they can be routinely produced in large quantities withwall thicknesses tunable in the range of 2–10 nm with an accuracy of 0.5 nm; *iii*) their LSPR peaks can be easily and precisely tuned to any wavelength of interest in the range of 600–1200 nm by simply controlling the amount of $HAuCl_4$ added to the reaction; *iv*) their hollow interiors can be used for encapsulation; *v*) their porous walls can be used for drug delivery, with the release being controlled by various stimuli; *vi*) their sizes can be readily varied from 20 to 500 nm to optimize biodistribution, facilitate particle permeation through epithelial tissues, or increasing drug loading; *vii*) their LSPR peaks can be dominated by absorption or scattering to adapt to different imaging modalities; and *viii*) other noble metals such as Pd and Pt can be incorporated into the walls during a synthesis to maneuver their optical properties.

During the past six years or so, we and our collaborators have actively explored the use of AuNCs in a variety of biomedical applications ranging from sensing to imaging, diagnosis, and treatment.[6] This review article only covers some of the most recent studies, with a focus

on their capabilities in theranostics. We start with a brief mechanistic discussion of the formation of AuNCs and our recent progress toward scaled-up production of AuNCs to reach the level needed for *in vivo* studies. We then elaborate on the unique chemical and optical properties of AuNCs. Finally, we used selected examples to highlight the merits of AuNCs in theranostic applications.

Synthesis

The invention of AuNCs was a result of two incidents occurring around the same time in our group: *i*) the development of a facile method based on polyol reduction for the synthesis of Ag nanocubes;[7] and *ii*) the teaching of general chemistry (by Xia) that happened to cover galvanic replacement. The galvanic replacement between Ag nanocubes and $HAuCl_4$ can be written as:

$$3Ag_{(s)} + AuCl_4^-{}_{(aq)} \rightarrow Au_{(s)} + 3Ag^+{}_{(aq)} + 4Cl^-{}_{(aq)} \quad (1)$$

This reaction occurs spontaneously owing to a favorable difference in electrochemical potential between Ag^+/Ag (0.80 V) and $AuCl_4^-/Au$ (1.00 V). We have systematically investigated this synthesis and detailed discussions can be found in our review.[6] Upon mixing with aqueous $HAuCl_4$, the Ag nanocubes were observed to go through four major stages of morphological and structural changes (Figure 1): *i*) initiation of Ag dissolution from a site with poor protection, such as a defect on the side face of a cube with sharp corners or the corner(s) of a cube with truncated corners; *ii*) dissolution of bulk Ag from the interior of the particle through the initial site(s) and concurrent deposition of Au on the rest of the surface; *iii*) formation of a nanobox (for a sharp cube) or nanocage (for a truncated cube) with uniform wall thickness due to alloying between Au and Ag; and *iv*) dealloying of Ag to generate pores on the walls of the nanobox, which eventually led to the formation of AuNCs.

For *in vivo* applications, one of the challenges is to produce AuNCs in large quantities (typically, >0.1 g) without sacrificing the uniformity in terms of size, shape, and optical response. As such, it is necessary to scale up the production of Ag nanocubes without compromising the quality. Although many methods have been developed for producing Ag nanocubes since our first publication in 2002, polyol reduction is at the foundation of all these techniques as it remains the best route in terms of quality and reliability.[8] In this method, ethylene glycol (EG) acts as both the solvent and a source of reductant as EG can be oxidized by the O_2 from air to form glycolaldehyde, an intermediate capable of reducing Ag^+ to Ag:

$$2Ag^+ + HOCH_2CHO + H_2O \rightarrow 2Ag + HOCH_2COOH + 2H^+ \quad (2)$$

In our early studies, $AgNO_3$ was used as a precursor to Ag and the synthesis was highly sensitive to many experimental conditions (e.g., impurities in EG and the amount of O_2 involved in the reaction), making it difficult to scale up the synthesis.[9] However, we recently discovered that the robustness and reproducibility of the synthesis could be greatly improved by switching from $AgNO_3$ to CF_3COOAg.[10] The synthesis based on this precursor was less sensitive to the batch of EG, and could be scaled up for routine, high-quality production of Ag nanocubes in relatively large quantities. Figure 2A shows a photograph of the experimental setup used for a typical synthesis in a 250 mL round-bottom flask. Figure 2B shows typical SEM and TEM images of one sample of Ag nanocubes (edge length: 40 nm) that was prepared at a scale of ~50 mg per batch. By monitoring the UV-vis spectra of the

reaction solution and stopping the synthesis at different time points, the edge length of the Ag nanocubes could be easily tuned from 30 to 70 nm. The size could be further extended to 200 nm by using Ag nanocubes as seeds for additional growth.[11] We have also obtained Ag nanocubes ~13 nm in size via overgrowth on single-crystal Au seeds 11 nm in diameter. [12]

The entire batch of Ag nanocubes (as an aqueous suspension after washing) could be placed in a 1000 mL flask and transformed into AuNCs by titration with $HAuCl_4$ at 90 °C. The extent of replacement could be readily monitored by taking UV-vis-NIR spectra of aliquots sampled from the solution. Figure 2C shows the shift in LSPR peak across the visible spectrum and into the NIR as the volume of $HAuCl_4$ was increased. Figure 2D shows a typical TEM image of AuNCs (edge length: ~50 nm) with LSPR peaked at 780 nm.

Typical AuNCs are composed of an Au-Ag alloy. If necessary, the remaining Ag can be selectively removed using aqueous etchants based upon $Fe(NO_3)_3$, NH_4OH, or H_2O_2.[13,14] During this treatment, nanoboxes are converted into thin-walled nanocages (Figure 1), accompanied by red-shifts in the LSPR peak. Alternatively, the surface of an Au-Ag alloyed nanobox or nanocage can be covered with pure Au through electroless deposition, together with a blue-shift for the LSPR peak.[15]

Imaging and Diagnosis

Owing to their extraordinarily large scattering and absorption cross sections,[16] AuNCs are superb optical tracers or contrast agents for imaging modalities such as dark-field microscopy,[17] optical coherence tomography (OCT),[18,19] PA tomography (PAT),[20–22] and multi-photon luminescence-based detection.[23,24] In this section, we will highlight two recent imaging demonstrations.

A. Two- and Three-Photon Luminescence (2PL and 3PL)

Solid Au can be optically excited to emit luminescence through a recombination of excited electrons in the *s*-*p* conduction band with holes in the *d*-band.[25] This emission is more pronounced for Au nanostructures, especially when they are excited by a laser in resonance with the LSPR peak in a 2-photon configuration, such as AuNCs[23] and nanorods.[26] This bright 2PL offers a simple means to examine and quantify the cellular uptakes of AuNCs with different surface coatings. However, since the LSPR peak of the AuNCs has to overlap with the excitation laser in 2PL, heat will also be generated due to the photothermal effect, causing adverse effects on the sample.[24] Figure 3, A and B, shows 2PL micrographs of KB cells before and after raster scanning the region of interest with a 760 nm femtosecond laser for 90 s. The arrows indicate areas where membrane blebbing occurred, and damage was confirmed by ethidium bromide staining (shown in green).

When Ag is included, AuNCs can emit strong photoluminescence under 3-photon excitation at a laser wavelength far away from the LSPR peak.[24] This less commonly observed 3PL appears to originate from the alloy composition of AuNCs because the 3PL from alloyed NCs (or nanoparticles) was an order of magnitude stronger than what was observed for nanoparticles made of pure Au or Ag. Figure 3, D and E, shows 3PL micrographs of KB cells before and after raster scanning the region of interest with a 1290 nm femtosecond laser for 90 s. Because no photothermal effect was involved in 3PL, we observed no membrane damage or photobleaching after scanning for 90 s. Another advantage for imaging with 3PL is that autofluorescence from the tissue can be completely suppressed at 1290 nm excitation, making it much easier to resolve the AuNCs. Figure 3, C and F, compares the 2PL and 3PL micrographs taken from the same liver tissue slice containing AuNCs. Clearly, 2PL showed a much stronger background than 3PL, primarily due to autofluorescence from the tissue.

B. Contrast Enhancement for PAT

PAT is a powerful hybrid imaging modality that combines the merits of both optical and ultrasonic imaging techniques, including strong optical absorption contrast and high ultrasonic spatial resolution. The contrast mechanism is based on differences in optical absorption.

We initially demonstrated AuNCs as intravascular contrast agents for PA imaging of cerebral cortex in a rat model.[20] In recent study, AuNCs were used as optical tracers for PA mapping of sentinel lymph nodes (SLN).[21] Such capability is a prerequisite for SLN biopsy (the standard procedure for axillary staging in breast cancer patients), where it is essential to precisely locate the SLN before a biopsy needle can be inserted for sample collection. Figure 4 illustrates the depth capability of SLN mapping by PA imaging after the administration of AuNCs. The PA image acquired at 28 min post-injection (Figure 4B) clearly reveals the vasculature and the SLN of the rat located at ~2 mm below the skin surface. Figure 4, C–E, show successive PA images of the same axillary region, each with an additional layer (~10 mm thick) of chicken breast tissue placed on top of the skin. The SLN could still be resolved at a depth of 33 mm, which is much deeper than the depth (~12 mm) of SLN in humans, demonstrating the feasibility of applying this system to human SLN mapping.

Therapeutic Applications

A. Cancer Targeting

Selectively delivering therapies to malignant tissues is of paramount importance in cancer treatment because it is a promising route to minimize damage to healthy tissue and consequently the harsh side effects from current broad-based treatments. Both passive and active targeting have been explored for delivering nanoparticles to a tumor site.

We have quantitatively assessed the passive targeting of AuNCs functionalized with PEG in a tumor mouse model.[27] The distribution of AuNCs in various organs indicates that there was very few AuNCs in normal tissue (0.95±0.24 %ID/g and 0.98±0.45 %ID/g at 24 h post-injection for muscle and fat, respectively), while the amount of AuNCs in tumor increased from 0.8±0.1 %ID/g at 1 h post-injection to 3.4±0.9 %ID/g at 24 h post-injection.

We also compared the passive and active targeting efficiencies of AuNCs for melanomas by *in vivo* PA imaging (Figure 5).[22] For active targeting, the AuNCs were derivatized with [Nle^4, D-Phe ^{7}]-α-melanocyte-stimulating hormone or [Nle^4, D-Phe^7]-α-MSH, a peptide that can selectively bind to the α-MSH receptors overexpressed on melanoma. The enhancement of PA signal in the melanoma was much stronger for the [Nle_4, D-Phe^7]-α-MSH-AuNCs (up to 36%) than for the PEG-AuNCs (up to 14% only), demonstrating an enhanced uptake of AuNCs by the tumor due to active targeting. Our ICP-MS analyses of the Au content also confirmed this dramatic increase.

B. Photothermal Cancer Treatment

We initially demonstrated the ability to destroy SK-BR-3 breast cancer cells *in vitro* by using the photothermal effect of anti-EGFR conjugated AuNCs.[28] In addition to fluorescence imaging, flow cytometry was also used to quantify the cellular damage caused by the photothermal effect under different experimental conditions, including a range of power densities and irradiation times.[29]

Most recently, we switched to a tumor mouse model to examine the efficacy of photothermal cancer treatment *in vivo* (Figure 6).[30] Tumor-bearing mice were administrated intravenously with 100 μL saline (as control) or 100 μL of 15 nM (or 9×10^{12} particle/mL) PEGylated AuNCs (for passive targeting). After 72 h post-injection, the tumor on the right

flank of each mouse was irradiated with a 808-nm continuous-wave (CW) diode laser at a power density of 0.7 W/cm^2 for 10 min. During the treatment, the tumors containing AuNCs were rapidly heated to temperatures over 55 °C while essentially no change was observed for the control. To evaluate the treatment response, we used [^{18}F] fluorodexoyglucose (^{18}F-FDG) positron emission tomography (PET) to monitor the changes in metabolic activity before and after photothermal therapy. For mice injected with AuNCs, there was a remarkable reduction in FDG uptake for the tumor on the right flank at 24 h post treatment as compared to no treatment. In contrast, the tumor on the left flank (without laser treatment) showed no significant difference for the FDG uptake at 0 h and 24 h. We normalized the signal of the right tumor to that of the left tumor to minimize the variation of FDG uptake at different time points (Figure 6E). The normalized values suggest a decrease in metabolic activity by 70%. For the control, the normalized value of FDG uptake showed no change before and after treatment.

C. Controlled Release of a Drug

We have turned AuNCs into a novel class of delivery vehicles by taking advantage of their hollow interiors, porous walls, and tunable LSPR properties. This feature is particularly interesting for theranostic applications because AuNCs can be monitored with optical imaging techniques while the drug is released at the targeted site.

In one study, we functionalized the surface of AuNCs with thermally-responsive polymers to control the release with NIR laser irradiation or high-intensity focused ultrasound (HIFU).[31,32] Figure 7A shows a schematic illustrating how this system works. The surface of AuNCs was coated with poly(N-isopropylacrylamide) (pNIPAAm) or its derivatives by means of Au-thiolate bonding. The polymer chains can change conformation in response to temperature variation at a point known as the low critical solution temperature (LCST).[33] The LCSTs of the smart polymers can be tuned from 32 to 50 °C through the incorporation of different amounts of acrylamide. When the AuNCs are irradiated by a NIR laser overlapping with the LSPR peak, the light will be absorbed and converted into heat through the photothermal effect. The polymer chains will collapse as the temperature increases beyond the LCST, opening the pores and thus releasing the pre-loaded drugs. When the laser is turned off, the temperature will drop and the polymer chains will relax back to the extended state, terminating the release. Similarly, drug release can also be triggered by heat generated by HIFU, which can penetrate more deeply into soft tissue.

Figure 7B shows the release profile of a PEG-conjugated alizarin dye from the copolymer-covered AuNCs by exposure to a nanosecond laser (790 nm) for different periods of time. The concentration of the released dye increased with irradiation time and power density (Figure 7C). The controlled release was further demonstrated *in vitro* with a commercial chemotherapeutic drug, doxorubicin (Dox). Figure 7D shows the effect of incubating Dox-loaded AuNCs with breast cancer cells. A significant reduction in cell viability was observed after irradiation with laser. For drug release from the HIFU-based system, we confirmed the release was localized to the focal volume of HIFU by taking fluorescence micrographs from gelatin phantoms containing dye-loaded AuNCs (Figure 7E). Only a small area around the focal volume of HIFU showed release of the dye after exposure for 20 min at a power of 10 W. We also demonstrated a penetration depth of up to 30 mm for this HIFU-induced system by placing chicken breast tissue on top of the phantom.

We recently demonstrated another new system by filling the hollow interiors of AuNCs with a phase-change material (PCM) such as 1-tetradecanol that has a melting point of 38–39 °C.[34] Since a PCM can reversibly change its physical state between solid and liquid over a narrow temperature range, it can confine pre-mixed drug molecules inside the AuNCs until the local temperature is increased beyond the melting point of the PCM, resulting in drug

release through diffusion (Figure 8A). As long as the drug is miscible with the PCM, it can be readily loaded into the hollow interiors of AuNCs as the PCM diffuses into the AuNCs. PCMs with a surfactant-like structure can be chosen, such as those containing both long hydrophobic tails and hydrophilic heads, to ensure good miscibility with different types of drugs. As shown in Figure 8B, we could control the release by varying the power of HIFU, and/or the duration of exposure to HIFU.

Concluding Remarks

Gold nanocages are well-suited for theranostic applications due to their multi-functional nature: they can serve as optical tracers or contrast agents for a variety of imaging and diagnostic techniques; they can kill cancer cells through the photothermal effect; and they can release drugs in a controlled manner in response to an external stimulus. Significantly, all these features can be readily integrated in the same system to fulfill both diagnostic and therapeutic requirements. For example, we recently developed an enzyme-sensitive, multimodal probe that allowed for tumor localization with PA imaging, evaluation of metastasis with NIR fluorescence, and treatment with the photothermal effect (Figure 9A).[35] In this case, we modified the surface of AuNCs with dye-labeled peptides cleavable by metalloproteases (MMPs) -- enzymes associated with cancer-cell invasion and metastasis. This hybrid system relies efficient, non-radiative energy transfer on to de-excite the dye bound to the surface. When no MMP-2 protease was present, the emission from the dye would be quenched. However, upon cleavage of the peptide in the presence of MMP-2, the dye was released from the AuNCs and fluorescence emission would be recovered. At a fixed incubation time of 12 h, a sensitivity of 0.01 U or 0.72 ng/mL was achieved for the detection of MMP-2 enzyme activity (Figure 9B). To demonstrate this dye-peptide-AuNC probe for *in vivo* fluorescence imaging, images of samples infused in agarose gel were taken after incubation with different concentrations of MMP-2, revealing a detectable level of MMP-2 at 0.1 U (Figure 9C).

We hope this account has given the reader a sense of the great potential of AuNCs for a diverse array of applications in both cancer diagnostics and treatment. As we and others continue to explore this promising material, the unique features of AuNCs and numerous ways in which the properties can be tuned will likely lead to the development of further exciting techniques and powerful combinations of existing ones.

Acknowledgments

This work was supported in part by an NIH Director's Pioneer Award (DP1 OD000798), a grant from NCI (1R01 CA138527), and startup funds from Washington University in St. Louis (WUSTL). We are grateful to our collaborators for their tremendous contributions to this project.

References

1. Cobley CM, Chen J, Cho EC, Wang LV, Xia Y. Gold nanostructures: A class of multifunctional materials for biomedical applications. Chem Soc Rev. 2011; 40:44–56. [PubMed: 20818451]
2. Weissleder R. A clearer vision for in vivo imaging. Nat Biotech. 2001; 19:316–317.
3. Seaman WB, Powers WE. Studies on the distribution of radioactive colloidal gold in regional lymph nodes containing cancer. Cancer. 1955; 8:1044–1046. [PubMed: 13261063]
4. Sun Y, Mayers BT, Xia Y. Template-engaged replacement reaction: a one-step approach to the large-scale synthesis of metal nanostructures with hollow interiors. Nano Lett. 2002; 2:481–485.
5. Sun Y, Xia Y. Mechanistic study on the replacement reaction between silver nanostructures and chloroauric acid in aqueous medium. J Am Chem Soc. 2004; 126:3892–3901. [PubMed: 15038743]
6. Skrabalak SE, Chen J, Sun Y, Lu X, Au L, Cobley C, Xia Y. Gold nanocages: synthesis properties applications. Acc Chem Res. 2008; 41:1587–1595. [PubMed: 18570442]

7. Sun Y, Xia Y. Shape-controlled synthesis of gold and silver nanoparticles. Science. 2002; 298:2176–2179. [PubMed: 12481134]
8. Skrabalak SE, Au L, Li X, Xia Y. Facile synthesis of Ag nanocubes and Au nanocages. Nat Protoc. 2007; 2:2182–2190. [PubMed: 17853874]
9. Zhang Q, Cobley C, Au L, McKiernan M, Schwartz A, Wen LP, Chen J, Xia Y. Production of Ag nanocubes on a scale of 0.1 g per batch by protecting the NaHS-mediated polyol synthesis with argon. App Mater Interfaces. 2009; 1:2044–2048.
10. Zhang Q, Li W, Wen LP, Chen J, Xia Y. Facile synthesis of Ag nanocubes of 30 to 70 nm in edge length with CF_3COOAg as a precursor. Chem Eur J. 2010; 16:10234–10239.
11. Zhang Q, Li W, Moran C, Chen J, Wen L, Xia Y. Seed-mediated synthesis of Ag nanocubes with controllable edge lengths in the range of 30–200 nm and comparison of their optical properties. J Am Chem Soc. 2010; 132:11372–11378. [PubMed: 20698704]
12. Ma Y, Li W, Cho EC, Li Z, Yu T, Zeng J, Xie Z, Xia Y. Au@ Ag core-shell nanocubes with finely tuned and well-controlled sizes, shell thicknesses, and optical properties. ACS Nano. 2010; 4:6725–6734. [PubMed: 20964400]
13. Lu X, Au L, McLellan J, Li Z, Marquez M, Xia Y. Fabrication of cubic nanocages and nanoframes by dealloying Au/Ag alloy nanoboxes with an aqueous etchant based on $Fe(NO_3)_3$ or NH_4OH. Nano Lett. 2007; 7:1764–1767. [PubMed: 17489641]
14. Zhang Q, Cobley CM, Zeng J, Wen L-P, Chen J, Xia Y. Dissolving Ag from Au-Ag alloy nanoboxes with H_2O_2: a method for both tailoring the optical properties and measuring the H_2O_2 concentration. J Phys Chem C. 2010; 114:6396–6400.
15. Sun Y, Xia Y. Increased sensitivity of surface plasmon resonance of gold nanoshells compared to that of gold solid colloids in response to environmental changes. Anal Chem. 2002; 74:5297–5305. [PubMed: 12403584]
16. Cho EC, Kim C, Zhou F, Cobley CM, Song KH, Chen J, Li Z, Wang LV, Xia Y. Measuring the optical absorption cross sections of Au-Ag nanocages and Au nanorods by photoacoustic imaging. J Phys Chem C. 2009; 113:9023–9028.
17. Hu M, Novo C, Funston A, Wang H, Petrova H, Zou S, Mulvaney P, Xia Y, Hartland GV. Dark-field microscopy studies of single metal nanoparticles: understanding the factors that influence the linewidth of the localized surface plasmon resonance. J Mater Chem. 2008; 18:1949–1960. [PubMed: 18846243]
18. Chen J, Saeki F, Wiley B, Cang H, Cobb MJ, Li ZY, Au L, Zhang H, Kimmey MB, Li X, Xia Y. Gold nanocages: Bioconjugation and their potential use as optical imaging contrast agents. Nano Lett. 2005; 5:473–477. [PubMed: 15755097]
19. Cang H, Sun T, Chen J, Wiley BJ, Xia Y, Li X. Gold nanocages as potential contrast agents for spectroscopic and conventional optical coherence tomography. Opt Lett. 2005; 30:3048–3050. [PubMed: 16315717]
20. Yang X, Skrabalak S, Li Z, Xia Y, Wang L. Photoacoustic tomography of a rat cerebral cortex in vivo with Au nanocages as an optical contrast agent. Nano Lett. 2007; 7:3798–3802. [PubMed: 18020475]
21. Song KH, Kim C, Cobley CM, Xia Y, Wang LV. Near-infrared gold nanocages as a new class of tracers for photoacoustic sentinel lymph node mapping on a rat model. Nano Lett. 2009; 9:183–188. [PubMed: 19072058]
22. Kim C, Cho EC, Chen J, Song KH, Au L, Favazza C, Zhang Q, Cobley CM, Gao F, Xia Y, Wang LV. In vivo molecular photoacoustic tomography of melanomas targeted by bioconjugated gold nanocages. ACS Nano. 2010; 4:4559–4564. [PubMed: 20731439]
23. Au L, Zhang Q, Cobley CM, Gidding M, Schwartz AG, Chen J, Xia Y. Quantifying the cellular uptake of antibody-conjugated Au nanocages by two-photon microscopy and inductively coupled plasma mass spectrometry. ACS Nano. 2010; 4:35–42. [PubMed: 19954236]
24. Tong L, Cobley CM, Chen J, Xia Y, Cheng JX. Bright three-photon luminescence from gold/silver alloyed nanostructures for bioimaging with negligible photothermal toxicity. Angew Chem Int Ed. 2010; 49:3485–3488.
25. Mooradian A. Photoluminescence of metals. Phys Rev Lett. 1969; 22:185–187.

26. Wang H, Huff TB, Zweifel DA, He W, Low PS, Wei A, Cheng J-X. In vitro in vivo two-photon luminescence imaging of single gold nanorods. Proc Natl Acad Sci. 2005; 102:15752–15756. [PubMed: 16239346]

27. Chen J, Yang M, Zhang Q, Cho EC, Cobley CM, Claus C, Kim C, Wang L, Welch MJ, Xia Y. Gold nanocages: A novel class of multifunctional nanomaterials for theranostic applications. Adv Funct Mater. 2010; 20:3684–3694.

28. Chen J, Wang D, Xi J, Au L, Siekkinen A, Warsen A, Li ZY, Zhang H, Xia Y, Li X. Immuno gold nanocages with tailored optical properties for targeted photothermal destruction of cancer cells. Nano Lett. 2007; 7:1318–1322. [PubMed: 17430005]

29. Au L, Zheng D, Zhou F, Li ZY, Li X, Xia Y. A quantitative study on the photothermal effect of immuno gold nanocages targeted to breast cancer cells. ACS Nano. 2008; 2:1645–1652. [PubMed: 19206368]

30. Chen J, Glaus C, Laforest R, Zhang Q, Yang M, Gidding M, Welch MJ, Xia Y. Gold nanocages as photothermal transducers for cancer treatment. Small. 2010; 6:811–817. [PubMed: 20225187]

31. Mustafa SY, Cheng Y, Chen J, Cobley CM, Zhang Q, Rycenga M, Xie J, Kim C, Song KH, Schwartz AG, Wang LV, Xia Y. Gold nanocages covered by smart polymers for controlled release with near-infrared light. Nat Mater. 2009; 8:935–939. [PubMed: 19881498]

32. Li W, Cai X, Kim C, Sun G, Zhang Y, Deng R, Yang M, Chen J, Achilefu S, Wang LV, Xia Y. Gold nanocages covered with thermally-responsive polymers for controlled release by high-intensity focused ultrasound. Nanoscale. 201110.1039/C0NR00932F

33. Hoffman AS. Hydrogels in biomedical applications. Adv Drug Deliv Rev. 2002; 43:3–12. [PubMed: 11755703]

34. Moon GD, Choi S-W, Cai X, Li W, Cho EC, Jeong U, Wang LV, Xia Y. A new theranostic system based on gold nanocages and phase-change materials with unique features for photoacoustic imaging and controlled release. J Am Chem Soc. 2011 in press.

35. Xia X, Yang M, Oetjen LK, Zhang Y, Li Q, Chen J, Xia Y. An enzyme-sensitive probe for photoacoustic imaging and fluorescence detection of protease activity. Nanoscale. 201110.1039/C0NR00874E

Biographies

Younan Xia received a B.S. in chemical physics from University of Science and Technology in China (USTC) in 1987, a M.S. in inorganic chemistry from University of Pennsylvania (with Prof. Alan G. MacDiarmid) in 1993, and a Ph.D. in physical chemistry from Harvard University (with Prof. George M. Whitesides) in 1996. After a short stint as a postdoctoral fellow, he started as an Assistant Professor of chemistry at the University of Washington (UW, in Seattle) in 1997. Hewas promoted to Associated Professor and Professor in 2002 and 2004, respectively. He moved to WUSTL in 2007 and is the James M. McKelvey Professor of biomedical engineering. His research interests include nanomaterials, nanomedicine, biomaterials, tissue engineering, self-assembly, colloids, surface science, and electrospinning.

Weiyang Li received both B.S. (2004) and M.S. degrees (2007) in chemistry from Nankai University, China. She is pursuing her Ph.D. in biomedical engineering with Prof. Xia at WUSTL.

Claire M. Cobley graduated with a B.S. in chemistry from Brown University (2006), a M.S. in chemistry from the UW (2007), and a Ph.D. in biomedical engineering from WUSTL (2010, with Prof. Xia). She is working with Prof. Joachim Spatz as a postdoc at the Max Planck Institute for Metals Research in Germany.

Jingyi Chen received a B.S. in chemistry from Sun Yat-Sen University, China (1997), a M.A. in chemistry from SUNY College at Buffalo (2002), and a Ph.D. in analytical chemistry with Prof. Xia from the UW (2006). She worked as a postdoc at Brookhaven

National Laboratory and then a Research Assistant Professor of biomedical engineering at WUSTL. In 2010, she started as an Assistant Professor of chemistry at the University of Arkansas, Fayetteville.

Xiaohu Xia received a B.S. in biotechnology from Xiamen University, China (2006), and stayed to pursue a Ph.D. degree in biomedical science. He joined the Xia group in 2009 as a jointly supervised student.

Qiang Zhang received a B.S. in materials physics (2005) and a Ph.D. in biological materials (2010) from USTC. He worked as a jointly supervised student in the Xia group from 2008–2010.

Miaoxin Yang received a B.S. in pharmacy from Shanghai Jiaotong University, China (2006) and a M.S. in chemistry from Nanyang Technological University, Singapore (2009). He is working with Prof. Xia at WUSTL as a graduate student in biomedical engineering.

Eun Chul Cho received a B.S. in polymer science and engineering from Sungkyunkwan University, Korea (1998). He received both M.S. (2000) and Ph.D. (2004) in polymer and interface science from Pohang University of Science and Technology (POSTECH), Korea. He was a postdoc with Prof. Xia at WUSTL for three years, and started as an Assistant Professor of chemical engineering at Hanyang University, Korea, in 2011.

Paige K. Brown received both B.S. (2008) and M.S. (2010) degrees in biological engineering from Louisiana State University, Baton Rouge. She is working with Prof. Xia at WUSTL as a graduate student in biomedical engineering.

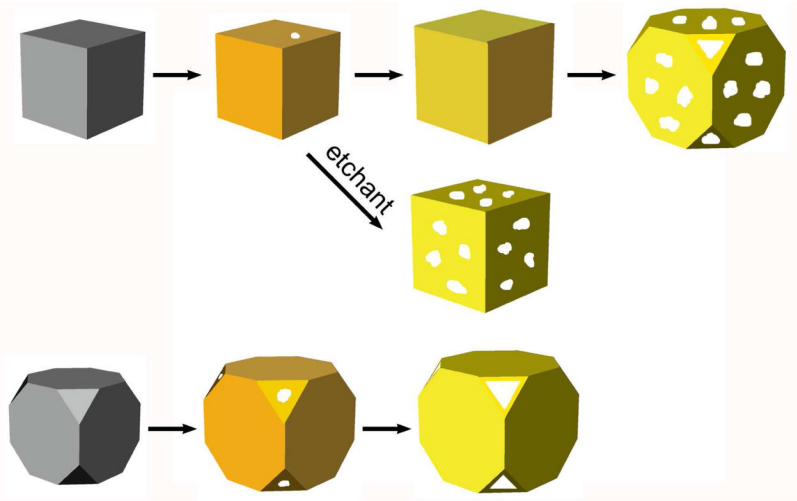

FIGURE 1.

Schematic illustrating the structural changes involved in the galvanic replacement reaction between aqueous $HAuCl_4$ and a Ag nanocube with sharp corners (top trace) or truncated corners (bottom trace). The middle trace shows selectively removal of Ag from the alloyed walls using an aqueous etchant such as $Fe(NO_3)_3$.

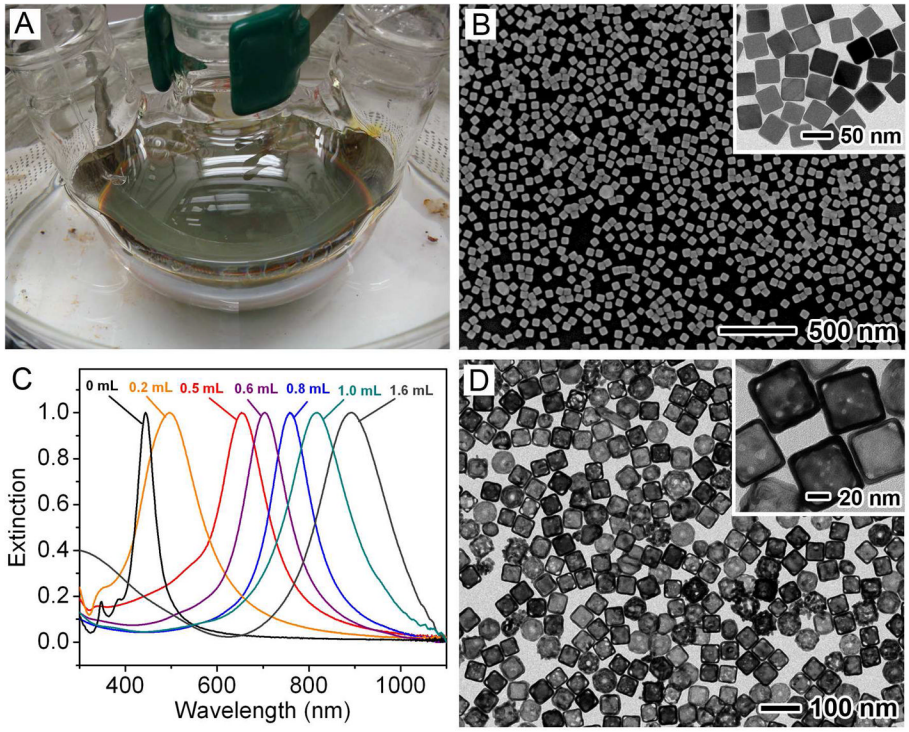

FIGURE 2.

(A) Photograph of an experimental setup for scaled-up synthesis of Ag nanocubes. (B) SEM image of the Ag nanocubes (edge length: ~40 nm). The inset shows a TEM image of the same sample. (C) UV-vis spectra of the samples obtained by titrating the Ag nanocubes with different amounts of aqueous $HAuCl_4$ solution. (D) TEM image of AuNCs (edge length: ~50 nm) with LSPR peaked at 780 nm.[27]

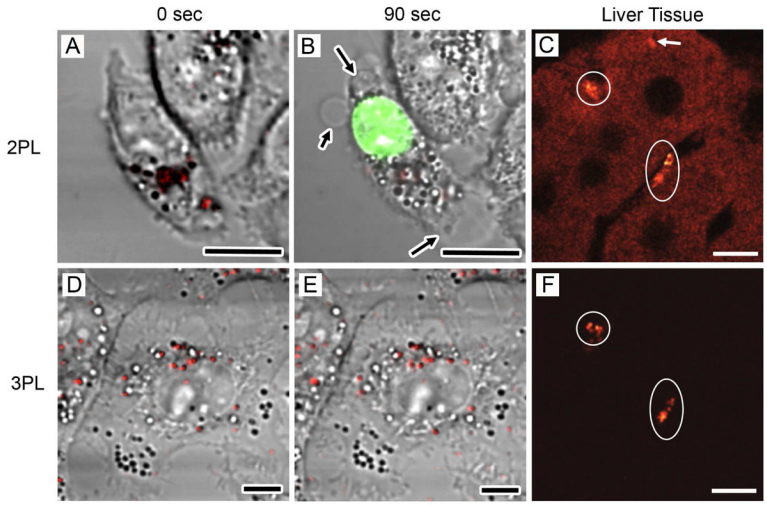

FIGURE 3.

Comparison of 2PL and 3PL imaging of AuNCs in KB cells and liver tissues. (A) 2PL image and (D) 3PL image of AuNCs (red) in KB cells before laser scanning. (B) Image of the same cell as in (A) after scanning with 760 nm femtosecond laser for 90 s. Membrane blebbing (black arrows) and compromised membrane integrity were revealed by ethidium bromide labeling (green). (E) 3PL image of the same cell as in (D) after scanning with a 1290 nm femtosecond laser for 90 s. No morphological change or plasma membrane damage was observed. (C) 2PL imaging of AuNCs (white circles) in liver tissue. (F) 3PL imaging in the same area as in (C). White arrow: Anomalously strong autofluorescence from tissue. Scale bars: 10 mm.[24]

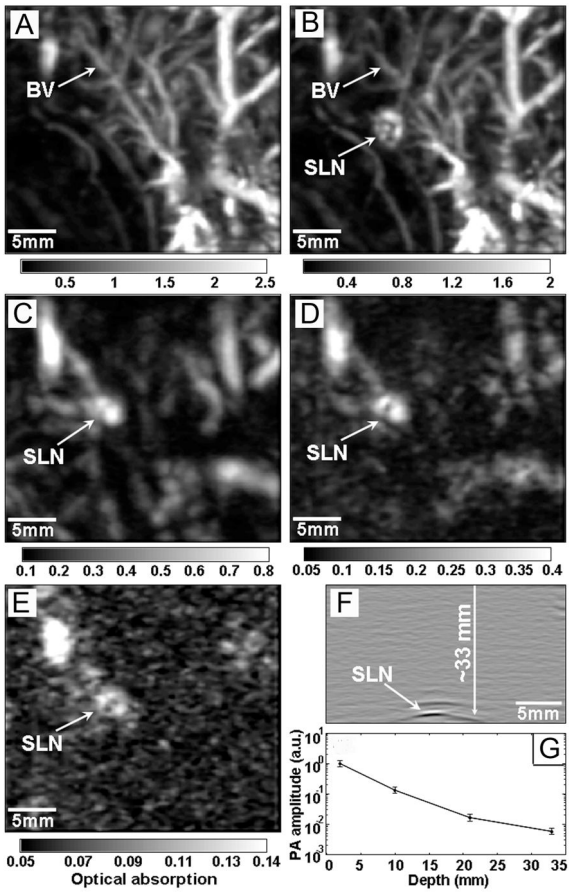

FIGURE 4.

Depth capability of SLN mapping with AuNCs. PA images taken (A) before and (B-E) after the injection of AuNCs for: (B) 28 min; (C) 126 min with a layer of chicken breast tissue placed on axillary region (imaging depth: 10 mm); (D) 165 min with the second layer of chicken breast tissue (imaging depth: 21 mm); (E) 226 min with the third layer of chicken breast tissue (imaging depth: 33 mm). (F) PA B-scan with 20 times signal averaging, showing the SLN located 33 mm deep. (G) The amplitude variations of PA signals over imaging depths. BV: blood vessel.[21]

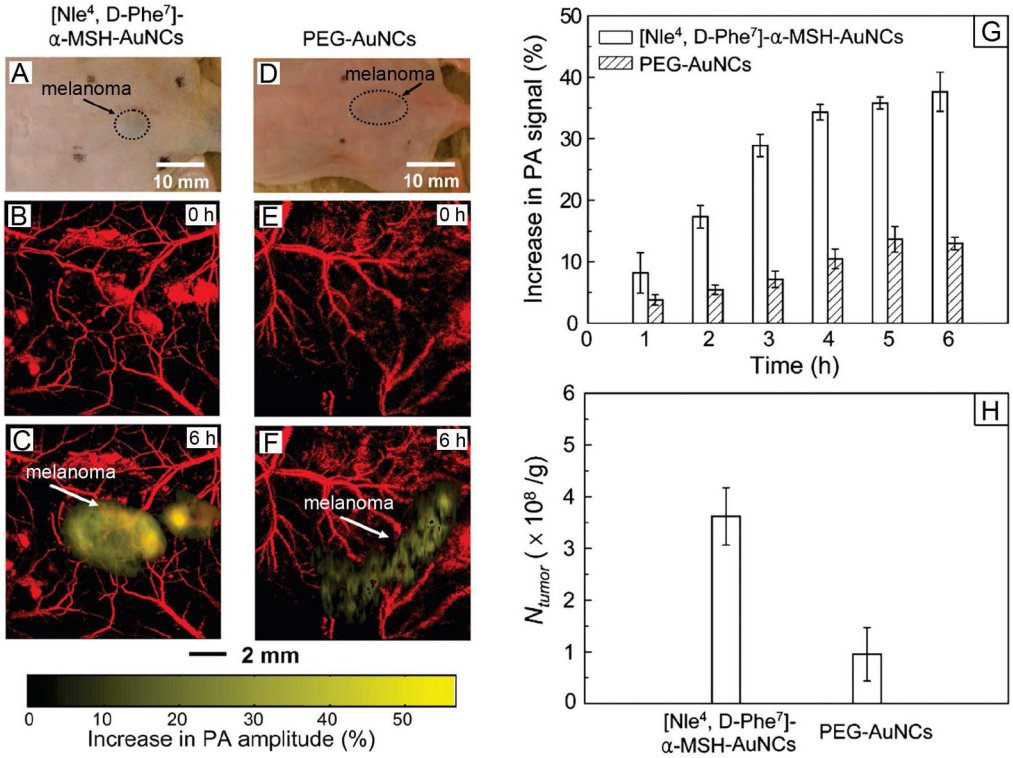

FIGURE 5.

(A, D) Photographs of nude mice transplanted with B16 melanomas before the injection of [Nle^4, D-Phe^7]-α-MSH- and PEG-AuNCs, respectively. PA images of the melanoma (B, E) before injection and (C, F) at 6 h post-injection of the two types of AuNCs. (G) Increase of PA amplitude in the melanoma tumors after intravenous injection of the AuNCs (n = 4 mice for each group) for different periods of time. (H) The average number (per unit tumor mass) of AuNCs accumulated in the melanomas dissected at 6 h post-injection and then measured by ICP-MS.[22]

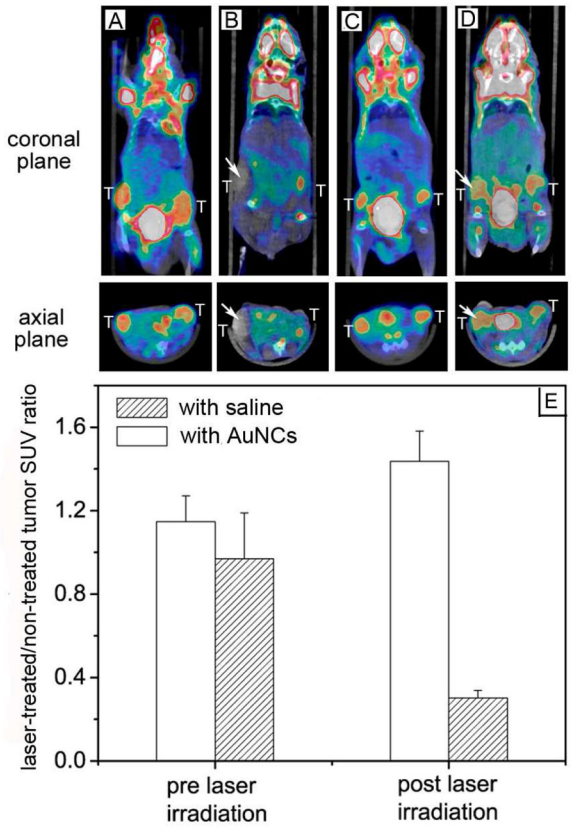

FIGURE 6.

^{18}F-FDG PET/CT co-registered images of mice intravenously administrated with either saline or PEG-AuNCs, followed by laser treatment: a nanocage-injected mouse (A) prior to and (B) after treatment; a saline-injected mouse (C) prior to and (D) after treatment. The white arrows indicates the tumors that were exposed to the diode laser at a power density of 0.7 W/cm^2 for 10 min. (E) A plot showing the ratios of laser-treated tumor to non-treated tumor for ^{18}F-FDG standardized uptake values (SUV, $P<0.001$).[30]

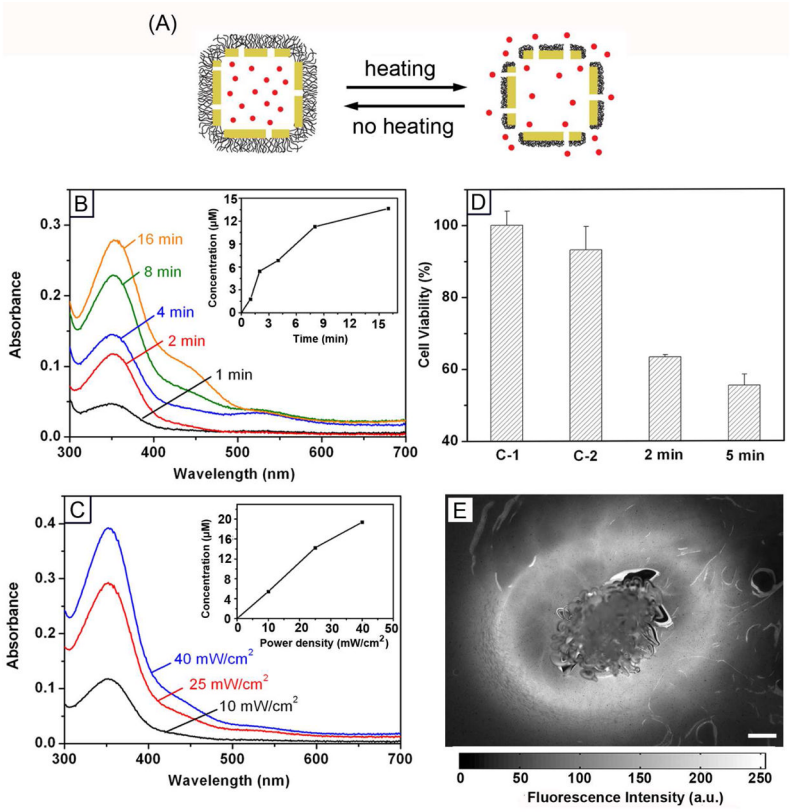

FIGURE 7.

(A) Schematic illustrating the release mechanism for AuNCs coated with smart polymers. (B) Absorption spectra of alizarin-PEG released from the copolymer-covered AuNCs upon exposure to a pulsed NIR laser (power density: 10 mW/cm^2) for 1, 2, 4, 8 and 16 min and (C) upon exposure to the laser for 2 min at 10, 25 and 40 mW/cm. The insets show the accumulated concentrations of alizarin-PEG released from the AuNCs. (D) Cell viability of samples after irradiation with the laser (C-1) for 2 min in the absence of AuNCs, (C-2) in the presence of empty AuNCs, and (2/5 min) for 2 and 5 min in the presence of Dox-loaded AuNCs.[31] (E) Fluorescence microscopy images of the gelatin phantom with dye-loaded AuNCs after exposure to HIFU at a power of 10 W for 20 min. Scale bars: 500 μm.[32]

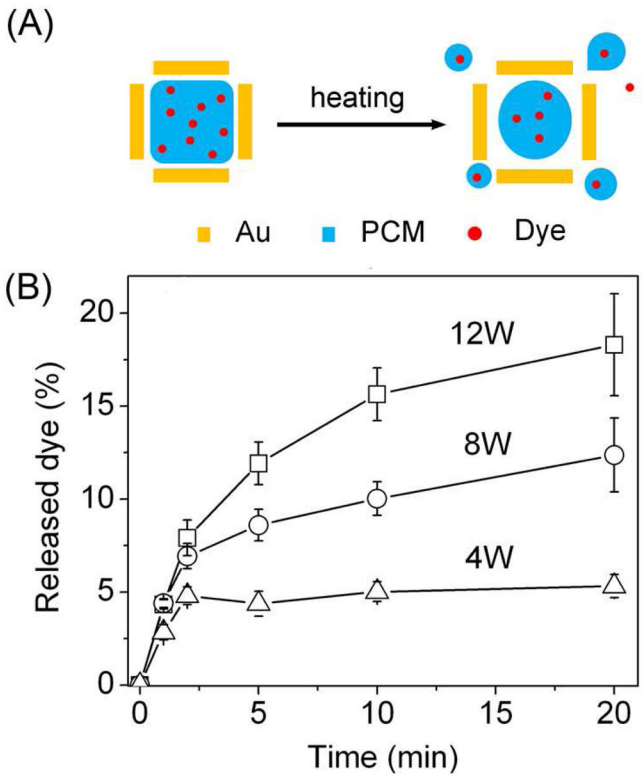

FIGURE 8.

(A) Schematic illustrating the release of dye from a AuNC loaded with dye-doped PCM. (B) Release profiles of the dye by exposed to HIFU at different applied powers.[34]

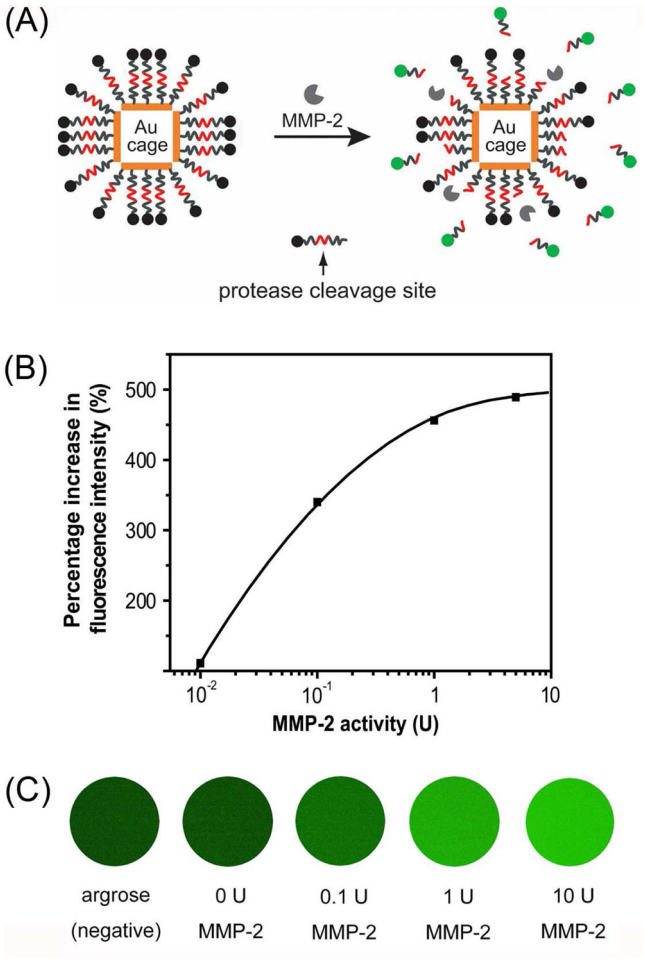

FIGURE 9.

(A) A schematic of the dual probe that could be activated by an enzyme. The probe is composed of a AuNC and fluorescent dyes linked together through a peptides cleavable by an enzyme. (B) Percentage increase in fluorescence intensity as a function of MMP-2 activity (20 fmol FITC-GKG*PLGVR*GC-AuNCs, incubation time: 12 h); (C) Fluorescence images of FITC-GKG*PLGVR*GC-AuNCs after incubation with different concentrations of MMP-2 at 37 °C for 12 h. The sample was mixed with 1.5% agarose to form gel for imaging.[35]